

Synthesis, Characterization, Thermal Analysis, DFT, and Computational/Anti-Corrosion Studies for New Azo Metal Complexes

Hanadi Mahdi Jarallah¹ and Safaa Hussein Ali^{2*}

¹Department of Chemistry, College of Education for Pure Science, University of Basrah, National Highway 216, Basrah 61004, Iraq

²Department of Physics, College of Education, Al-Shatrah University, Al-Dawaia Rd. 105, Al-Shatrah 64007, Iraq

* **Corresponding author:**

tel: +964-7808901830

email: safaa.ali@shu.edu.iq

Received: October 29, 2024

Accepted: February 1, 2025

DOI: 10.22146/ijc.101069

Abstract: Two new azo-substituted ligands (L1 and L2) were synthesized in a two-step reaction involving condensation between diazonium salt and hydroxyanisole. L1 is (E)-2-(tert-butyl)-6-((4-chlorophenyl)diazenyl)-4-methoxyphenol, and L2 is (E)-2-((3-(tert-butyl)-2-hydroxy-5-methoxyphenyl)diazenyl)benzoic acid. These ligands were employed to synthesize four new bidentate azo metal complexes $[MCl_2(L_x)]$ ($x = 1$ or 2 , $M = Ni(II)$ or $Cu(II)$). The prepared compounds were characterized using various structural analysis techniques, including IR, EI-mass, ¹H-NMR, ¹³C-NMR, and thermogravimetric analysis (TGA). The results confirmed that the ligands coordinate to the metal ion in a bidentate manner through the nitrogen atom of the azo group, the deprotonated phenolic oxygen in the case of L1, and the carboxylic oxygen in the case of L2. A theoretical study was also performed to predict the chemical reactivity and stability of the prepared ligands and their metal complexes. A set of mathematical calculations was employed to describe the full geometry optimizations using density functional theory (DFT), including chemical hardness (η), electronic chemical potential (μ), and electronegativity (χ). The small energy gap calculated between the highest occupied molecular orbital and least unoccupied molecular orbital energies indicates charge transfer within the complexes. These computational calculations suggest that the title compounds are promising candidates as corrosion inhibitors.

Keywords: azo; corrosion; computational studies; density function theory; metal complex

■ INTRODUCTION

Azo compounds have received considerable attention over the last two decades [1-3] as it has been used extensively as pigments and dyes because of its colored properties [4-6]. Chemically, azo species are distinguished by the presence of the ($R_1-N=N-R_2$) functional group [7]. This group plays a fundamental role in stabilizing dyes by forming a conjugated system, which absorbs visible light frequencies and produces colored compounds [8-10]. Coordinating azo compounds with metal ions enhanced stability, tunable optical properties, and geometrical features [11-12]. In addition to the electron donor/acceptor properties of the ligand, structural-functional groups and the position of the ligand in the coordination sphere [13-14].

Azo compounds, particularly in the form of aromatic

azo metal complexes, have been utilized in a wide range of promising applications in many areas, such as optical materials [15], biomedical materials [16], nanomaterials [17], textile [18], printing [19], paints and coatings [20], plastics [21], colorimetric sensors [22], photonic devices [23], art conservation [24], corrosion inhibitors [25], and electrochromic materials [26]. In all these applications, the intense and stable colors of azo metal complexes are a significant advantage [27]. The ability to fine-tune the color through structural modifications of the ligands and the choice of metal ions allows for versatile applications across different industries and technological fields where color plays a critical role in functionality and aesthetics [28]. Moreover, azo metal complexes exhibit diverse catalytic activities that stem from the combination of the metal center's reactivity

and the electronic properties of the azo ligand [29]. These metal complexes have garnered interest in catalysis due to their unique structural and electronic properties, which can influence their catalytic activity in various organic transformations including oxidation/reduction reactions [30], C–C and C–N bond formation [31], hydrogenation [32], polymerization [33], asymmetric catalysis [31], photocatalysis and bioinspired catalysis [28].

Inspired by enzymatic processes, azo metal complexes have been designed to mimic enzymatic catalysis in organic transformations [31]. These complexes can offer advantages such as substrate specificity [33], catalytic efficiency [30], and mild reaction conditions [31]. Azo metal complexes with specific electronic transitions can be incorporated into devices such as organic light-emitting diodes, where their absorption and emission properties can influence device efficiency and color output [23]. Certain azo metal complexes exhibit nonlinear optical properties, which are crucial for applications in telecommunications, laser technology, and optical data storage [10,15]. Azo metal complexes can act as sensitive probes for detecting metal ions and other analytes. Changes in their optical properties or fluorescence in the presence of specific ions can be used to develop selective sensors [8-9]. Azo metal complexes have potential applications in biomedicine, such as in drug delivery systems where external stimuli like light can trigger the release of bioactive molecules. The reversible photoisomerization of azo groups allows for controlled drug release in response to specific conditions. Thus, significant attention was paid to synthesizing new azo metal complexes [3-4,11-12,14].

Ongoing research continues to explore and optimize these azo-metal complexes for anticorrosion and catalytic applications, aiming to develop efficient and selective corrosion inhibitors. In this study, we synthesized two new azo dye ligands, L1 and L2, (L1 is (*E*)-2-(*tert*-butyl)-6-((4-chlorophenyl)diazenyl)-4-methoxyphenol, and L2 is (*E*)-2-((3-(*tert*-butyl)-2-hydroxy-5-methoxyphenyl)diazenyl)benzoic acid) and used them to prepare four metal complexes with Ni(II) and Cu(II). The coordination compounds were fully characterized using various analytical and spectroscopic techniques to gain

deeper insights into their thermal and catalytic properties. Theoretical and computational studies, including density functional theory (DFT) calculations, play a crucial role in advancing our understanding of the anticorrosion properties of metal azo compounds in several significant ways, such as electronic structure. Copper and nickel are crucial metals widely used in essential components of engines, electronic devices, cooling systems, pipelines, and other applications [34-35]. Oxide accumulation is the primary cause of leaks and other corrosion issues [36]. Therefore, exploring new materials to protect these metals, particularly in air conditioning systems, has become increasingly important, especially during prolonged heat waves driven by climate change. Studies on copper and nickel corrosion problems are still very limited in comparison with steel corrosion issues [34]. Azo metal complexes are selected as corrosion inhibitors based on several factors. These compounds can be simply synthesized at a lower cost [1]. They possess numerous active sites with electron donation abilities [4]. Moreover, azo dyes exhibit a pronounced ability to mitigate the sweet corrosion of the metal surface [36]. Azo metal complexes can catalyze reduction reactions, promoting the conversion of functional groups such as nitro groups to amines or carbonyl groups to alcohols [31]. The metal center in these complexes can facilitate electron transfer processes critical for anticorrosion and coating metal surfaces [25].

bonding analysis, geometrical optimization, energies, and corrosion inhibition mechanism. These computational studies revealed the title compounds have promising anti-corrosion properties.

■ EXPERIMENTAL SECTION

Materials

The analytical grades of *p*-chloroaniline, anthranilic acid, and 3-*tert*-butyl-4-hydroxyanisole were purchased from Sigma Aldrich and used as received without any further purification.

Instrumentation

The Fourier-transform infrared (FTIR) spectroscopy was used for the title compounds on the

Shimadzu spectrophotometer from 4000–400 cm^{-1} at 25 °C using KBr plates. ^1H - and ^{13}C -NMR spectra were recorded in $\text{DMSO-}d_6$ on a Bruker (500 MHz) spectrophotometer. EI-mass spectra were recorded on Agilent technology of 70 eV at the Central Chemical Analysis Lab, College of Science, University of Tehran, Iran. Thermal analysis data were collected using a TA instrument (SDT Q600 V20.9 Build 20) using standard 90 μL alumina metal pans under Ar (50 mL/min) from 25–800 °C (with a ramp of 10 °C/min). Melting points were determined in glass capillaries.

Procedure

Ligands synthesis

The *p*-chloroaniline or anthranilic acid (0.638 g or 0.685 g, 5 mmol) was dissolved in (10 mL) of distilled water that acidify with 1 mL of HCl and cooled down in an ice bath (0–5 °C) with a continuous stirrer. The pH of the resulting solution was adjusted with 0.38 g of NaNO_2 , dissolved in 10 mL of distilled water, which was added dropwise. This mixture was continually stirred in an ice bath, and 3-*tert*-butyl-4-hydroxyanisole (0.901 g, 5 mmol) was gradually added (Fig. 1) [3-4]. The resulted mixture was chilled in an ice bath and stirred for 1 h until a precipitate was formed. The final product was filtered, recrystallized from ethanol, and dried in the oven at 50 °C for 24 h. In the case of L1, an orange solid was obtained with a yield of 87% and a melting point of 100–102 °C. For

L2, a red solid was collected with a yield of 81% and a melting point of 182–184 °C.

Preparation of azo dyes metal complexes MCl_2L (1-4)

The complexation process between the prepared ligands (L1 and L2) and metal ions (Ni and Cu) was achieved by adding 10 mL of hot ethanolic solution of 1 mmol (0.237 g) of $\text{NiCl}_2 \cdot 6\text{H}_2\text{O}$ or 1 mmol (0.17 g) $\text{CuCl}_2 \cdot 2\text{H}_2\text{O}$ to a hot ethanoic solution containing 1 mmol (0.31 g) of L1 or L2 (0.32 g) that charged in a 50 mL round bottom flask (Fig. 2). The mixture was basified by adding 2 mL of triethylamine. The reaction mixture was then refluxed for 3–4 h. The obtained solution was cooled down for 1 h in the freezer [10,12]. The formed precipitate was filtered, washed with ethanol, then with diethyl ether, and dried in air. The thermogravimetric analysis (TGA) of Ni(II) and Cu(II) complexes was recorded at room temperature up to 700 °C under N_2 gas flow and a heating rate suitably controlled at 10 °C/min. The stages of decomposition, temperature range, TGA peak temperature, and decomposition product loss were also found, and the calculated mass loss percentages were analyzed.

Theoretical studies

Gaussian 09W software package was employed to explore the molecular conformation of the ligand and its complexes because of the absence of an X-ray single crystal structure analysis. The geometrical structures were

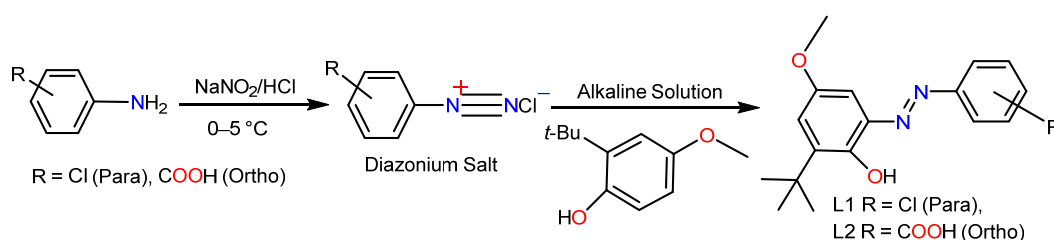


Fig 1. Synthesis of azo compounds L1 and L2

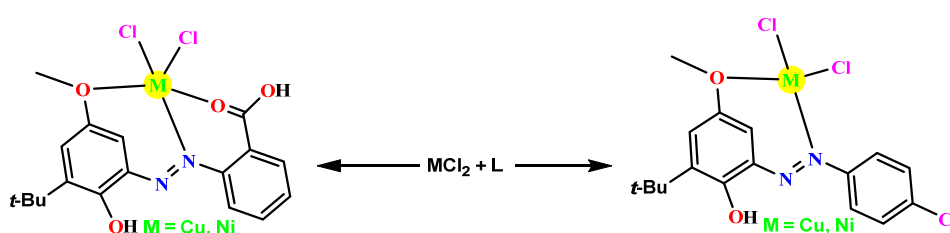


Fig 2. Synthesis of azo metal complexes

optimized using the DFT method with the functional approach of B3LYP exchange-correlation. Gaussian09W program packages installed on a personal computer (Huawei, Core i5, Windows 10) was used to collect the computational data. The Becke's hybrid functional with three parameter LYP correlation functional (B3LYP). The basis set of 6-31G(d,p), the robust function of the hybrid family, was employed for theoretical calculations. GaussView 5.0 was used to display the Gaussian program's collected files [37-38].

■ RESULTS AND DISCUSSION

The two azo-substituted ligands (L1 and L2) were employed to synthesize four new metal azo complexes $[MCl_2(L)]$. The substituted-azo compounds and their metal complexes were synthesized following the reaction schemes in Fig. 1 and 2.

Chemical Characterization of Ligands (L1 and L2)

FTIR spectra

The FTIR spectrum of L1 (Fig. S1) shows different characteristic bands. A weak and broadband at 3450 cm^{-1} is attributed to OH stretching vibration. Moreover, strong bands at 2950 and 2912 cm^{-1} are attributed to the asymmetric and symmetric stretching vibration of aliphatic C-H of butyl moiety. Furthermore, the sharp band at 1444 cm^{-1} indicated the presence of the azo ($-N=N-$) group. Strong bands at 1309 and 1139 cm^{-1} were assigned to C-N and C-O stretching vibration, respectively. A strong band at 837 cm^{-1} indicated the presence of C-Cl. These vibrations are consistent with previous studies [3-4]. Fig. S2 of the FTIR spectrum highlights key peaks that confirm the synthesis of ligand L2. A broad band at 3452 cm^{-1} is attributed to bonded OH. The strong band appeared at 1683 cm^{-1} and was assigned to the stretching vibration of the C=O group. The band with medium intensity at 1452 cm^{-1} might be related to the $-N=N-$ vibration. A strong band at 1257 cm^{-1} is attributed to C-N stretching, while another strong band at 1145 cm^{-1} is attributed to C-O stretching. Stretching bands in Fig. S2 are comparable with previous reports [5-6].

$^1\text{H-NMR}$

The $^1\text{H-NMR}$ spectrum of L1 (Fig. S7) confirms the suggested structure. The nine equivalent protons of the (*t*-

Bu) group appear as a singlet at δ 1.45 ppm and the OCH_3 protons at δ 3.78 ppm. The aromatic protons appear at δ 7.02–8.15 ppm and the OH signal at δ 11.09 ppm [3,10]. Fig. S8 shows the following signals that confirm the chemical structure of L2. A singlet peak at δ 1.38 ppm was attributed to (*t*-Bu) protons. Another singlet appears at δ 3.78 ppm assigned to OCH_3 protons. In comparison, the aromatic protons appeared as multi-signals at δ 6.94–7.89 ppm. There are two signals in the high field. The first one at δ 13.52 ppm was attributed to phenolic OH proton and the other at δ 13.82 ppm for carboxylic proton, respectively [11-13].

$^{13}\text{C-NMR}$

The $^{13}\text{C-NMR}$ results (Fig. S9 and S10) of the ligands (L1 and L2) are another evidence that confirms the successful formation of azo compounds. $^{13}\text{C-NMR}$ spectra showed some characteristic peaks, such as at δ 55.81 and 55.87 ppm assigned to the carbon atoms of OCH_3 groups for L1 and L2, respectively. Carbon atoms (C_1 and C_2) of (*t*-Bu) groups represented two peaks at δ 29.62 and 35.27 ppm, as well as 29.5 and 35.30 ppm for each ligand (L1 and L2), respectively. L2 spectrum (Fig. S10) has a characteristic peak at δ 168.23 ppm related to the carbon atom of the $-\text{COOH}$ group. Multi-signals at δ 101.26–152.42 ppm are assigned to carbon atoms of aromatic rings [16,35].

Mass spectra

The mass spectrum of L1 (Fig. S11) shows an intense peak (base peak) at m/z 318.2, which is attributed to the molecular ion. In addition, the peak at m/z 320 is less intensity compared with the molecular ion peak at m/z 318, confirming the presence of one chlorine atom (Isotope 37). The peak at m/z 303 (R.I = 60%) was attributed to the loss of one methyl group from molecular ion. Another intense peak (R.I = 69%) at m/z 192 attributed to ion resulted from the loss of Ph-Cl moiety from the molecular ion [3,5,10].

The mass spectrum of L2 (Fig. S12) shows the molecular ion at m/z 328 (base peak), confirming the suggested formula and the high stability of the molecular ion. The relative intensity of the peak at m/z 310 is attributed to the loss of H_2O from the molecular ion, also, the spectrum showed an intense peak at m/z 192,

which is attributed to the loss of Ph-COOH [4,6].

Azo Dyes Metal Complexes Analysis

The physical properties of the prepared compounds **1–4** are shown in Table 1. Title compounds **1–4** were structurally characterized with a set of different spectroscopic techniques, such as molar electrical conductivity, FTIR, ¹H-NMR, ¹³C-NMR, and mass spectra.

Molar electrical conductivity

The low molar conductance values measured in DMF (10⁻³ M) solution fall in the ($\Lambda_M = 17\text{--}27 \text{ S cm}^2 \text{ mol}^{-1}$) range Table 1, indicating, the weak electrolytic nature of these complexes. Molar electrical conductivity is affected by the substituted groups on ligands, such as containing donating and accepting groups on the benzene ring [1-2].

FTIR spectra

FTIR spectroscopy is a very important technique for determining the type of complexation. Fig. S3-S6 showed the shift of azo group vibration to a lower frequency, indicating the participation of one of the azo nitrogen atoms in coordination with the metal ion. The spectra of metal complexes showed medium and weak bands at

3441–3493 cm⁻¹, suggesting the existence of coordinated and lattice water molecules in the structure of metal complexes [3-5].

Thermal analysis

The TGA studies were performed to highlight the thermal behavior of the complexes **1–4**. The thermal decomposition process of the metal complexes generally involves three consecutive stages (dehydration, ligand pyrolysis, and inorganic residues). Such information can be significant information about thermal properties, intermediate nature, and final products of thermal decomposition stages. Fig. S13-S16 and Table 2 showed the thermal analysis of complexes **1–4**, respectively [20,39-40].

[NiCl₂L1] (1). The TGA curve (Fig. S13) shows 3 stages of mass loss, indicating continuous decomposition. The first peak at 189 °C suggests the compound is thermally stable up to 253 °C. In the next stage (306–406 °C), the thermal curve shows a mass loss of up to 14% due to the elimination of a C₂H₅Cl fragment. The final decomposition stage, occurring between 441–540 °C, is attributed to the loss of a C₃H₉N fragment.

Table 1. Physical properties of the prepared compounds (**1–4**)

Complexes	Color	m.p. (°C)	Yield (%)	Λ_m (S cm ² mol ⁻¹)
[NiCl ₂ (L1)] (1)	Brown	298–300	71	27
[CuCl ₂ (L1)] (2)	Black	240–242	69	18
[NiCl ₂ (L2)] (3)	Dark brown	296–298	73	17
[CuCl ₂ (L2)] (4)	Brown	294–296	77	21

Table 2. Thermogravimetric analysis of complexes (**1–4**)

Complexes	Stage	TG range (°C)	Weight loss %		Assignment	Metallic Residue
			Found	Calc.		
[NiCl ₂ (L1)]	1	189–253	9.50	10.04	2.5H ₂ O	Ni; % 12.0 Found; % 12.9 Calc.
	2	306–406	15.13	14.38	C ₂ H ₅ Cl	
	3	441–540	13.51	13.18	C ₃ H ₉ N	
[CuCl ₂ (L1)]	1	177–244	9.70	9.93	2.5H ₂ O	Cu; % 12.5 Found; % 14.0 Calc.
	2	293–371	37.30	37.56	C ₆ H ₁₈ N ₂ O	
	3	443–509	10.62	11.14	CH ₃ Cl	
[NiCl ₂ (L2)]	1	225–349	20.49	19.92	C ₂ H ₄ N ₂ O + 2H ₂ O	NiO + 14C; % 49.00 Found; % 49.08 Calc.
	2	348–444	12.76	12.69	C ₂ H ₃ Cl	
[CuCl ₂ (L2)]	1	258–327	53.83	52.82	C ₁₃ H ₁₂ N ₂ O ₂	CuO + 4C; % 23.0 Found; % 22.4 Calc.
	2	444–498	10.18	10.15	CH ₃ Cl	

[CuCl₂L1] (2). The TGA curve of the bulk sample (Fig. S14) also showed 3 stages of decomposition similar to complex **1** as the first started at 177 up to 244 °C, corresponding to C₂H₄O eliminated. TGA shows a change in the slope at 293–371 °C with 37.56% mass loss related to C₆H₁₈N₂O loss. Thermal calculations indicated that the final stage, occurring at 443–509 °C, is attributed to the loss of a CH₃Cl fragment.

[NiCl₂L2] (3). The thermogram showed 2 stages (Fig. S15) of thermal decomposition patterns. The first stage at 225–349 °C is due to the C₄H₈N₂O fragment loss. The resulting compound follows the TGA plateau up to 444 °C, after which the curve exhibits a mass loss of 12.69%.

[CuCl₂L2] (4). The thermo-analytical curve (TGA curve) (Fig. S16) revealed that the title compound undergoes 2 decomposition stages. It is interesting to note that the mass loss of the compound remains constant up to a temperature of 327 °C. Thereafter, the first stage started at 258 °C. This confirms the C₁₃H₁₁ClN₂O elimination. Later, the compound experienced a mass loss of about 498 °C, which was related to CH₃Cl loss.

Quantum Chemical Calculations

Computational calculations and theoretical studies or DFT were conducted to explore the electronic properties and global reactivity parameters of the titled compounds L1, L2, and the metal complexes (**1–4**). The electronic properties include total energy, E_{HOMO}, E_{LUMO}, and energy gap (E_g). While a set of reactivity parameters also studied such as electronegativity (χ), ionization potential (IP), electron affinity (EA), chemical potential (μ), global hardness (η), and global softness (ς). In

addition to these factors, the electronic surface potential (ESP) and the electronic potential map (EPM) have been calculated for the title compounds such as L1 and [CuCl₂(L1)] (Fig. 3 and 4). The highest occupied molecular orbital (HOMO) and the least unoccupied molecular orbital (LUMO) were used as references to calculate some quantum chemistry parameters through the values of the energies of the HOMO and the LUMO according to Koopman's theorem [41].

IP is the energy required to remove an electron from a molecule [36,42]. It is related to the energy of the E_{HOMO} through the Eq. (1).

$$IP = -E_{HOMO} \quad (1)$$

Table 3 clearly shows how the E_{HOMO} values increased for metal complexes compared to the E_{HOMO} values for L1 and L2 [36]. The inhibitor's anti-corrosion capability relies on the inhibitor's electron donation capacity, which is linked to its E_{HOMO}. Molecules with high E_{HOMO} can donate electrons to the metal's corresponding lower molecular orbital. Thus, the adsorption of the inhibitor molecule onto metal surfaces strongly inhibits corrosion. Consequently, anti-corrosion

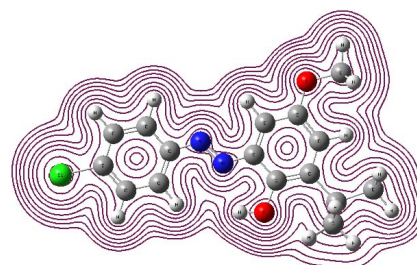


Fig 4. Electrostatic potential map of L1

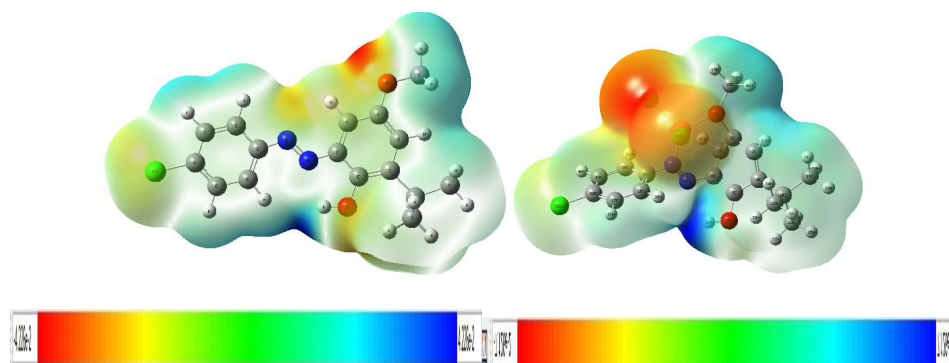


Fig 3. Electronic surface potential of (a) L1 ((-4.22) – (+4.22) au) and (b) [CuCl₂(L1)] ((-7.12) – (+7.12) au)

capability can be enhanced by accelerating or improving the electron transfer process. Electron affinity is the energy released when a proton is added to a system as it correlates to E_{LUMO} according to Eq. (2) [36,43].

$$EA = -E_{LUMO} \quad (2)$$

Table 3 shows the E_{LUMO} values, indicating that the inhibitors (L1, L2, and complexes 1–4) can accept electrons from Cu or Ni, thereby enhancing their inhibitory effect on the metal surfaces. Electronegativity is described as the electron attraction power of an atom towards itself Eq. (3) [44].

$$\chi = I + \frac{A}{2} \quad (3)$$

The electronegativities of the molecule are in equilibrium with its constituent atoms [45]. The electronegativity values of the molecules under study are summarized in (Table 3). Eq. (4) and (5) describe chemical hardness (η) and softness, respectively. Chemical hardness is defined as a measure of convexity of the $E(N)$ function and quantifies the stability of the neutral state of the atom. While chemical softness is the opposite of hardness [36].

$$\eta = I - \frac{A}{2} \quad (4)$$

$$\sigma = \frac{1}{\eta} \quad (5)$$

The η is a crucial tool for understanding reaction mechanisms and predicting the products of chemical reactions [36,44]. Acid and base theory has suggested a link between molecular hardness and the geometric mean of the chemical hardness of its component atoms [46].

Also, there is a direct relation between chemical stability and hardness according to the maximum hardness principle [47]. Chemical compounds with low bandgap have strong anticorrosion efficiency because of their low hardness values. Thus, hard chemical compounds should have a large energy gap and soft chemical compounds should have a small energy gap [48].

The E_g is defined as the difference between a molecule's E_{LUMO} and E_{HOMO} . It is related to the inhibitor's adsorption on the metal surface. As expected, a decrease in the ΔE of the inhibitor can enhance the binding between the metal surface and the inhibitor because of the decreasing energy required to remove the electron from the highest occupied molecular orbital [49]. According to Table 3, the E_g value indicates L1 and L2 molecules perform better than complexes 1–4 due to their lower energy gaps and stronger reactivity.

$$E_g = E_{LUMO} - E_{HOMO} \quad (6)$$

The number of transferred electrons from the inhibitor (L1 and L2) to the metal surface (Cu and Ni) (ΔN) was calculated using Eq. (7);

$$\Delta N = \frac{\chi_M - \chi_{inh}}{2(\eta_M + \eta_{inh})} \quad (7)$$

where χ_M and χ_{inh} are the absolute electronegativity of metal and inhibitor, respectively; η_M and η_{inh} are the absolute hardness of metal and the inhibitor, respectively [44]. M is Cu or Ni metal.

ΔN can be used as an indicator for the electron-transfer capacity of the inhibitor. An inhibitor's ability to donate electrons increases along with its inhibitory

Table 3. The calculated quantum chemical parameters of L1, L2, and complexes 1–4

Parameters	L1	L2	[NiCl ₂ L1]	[CuCl ₂ L1]	[NiCl ₂ L2]	[CuCl ₂ L2]
Total Energy	-3.7524	-3.0146	-9.9960	-1.0343	-9.6217	-9.9810
E_{HOMO} (eV)	-5.6965	-5.4455	-5.6221	-6.3165	-4.9835	-5.1821
E_{LUMO} (eV)	-2.6216	-2.7279	-4.0394	-3.9008	-3.9556	-3.2831
ΔE_{gab}	3.0752	2.7181	1.5836	2.4162	1.0287	1.8994
IP	5.6967	5.4463	5.6234	6.3166	4.9835	5.1821
EA	2.6213	2.7282	4.0396	3.9008	3.9554	3.2827
χ	4.1589	4.0868	4.8311	5.1086	4.4695	4.2325
η	1.5376	1.3588	0.7916	1.2078	0.5148	0.9497
ς	0.6504	0.7359	1.2633	0.8286	1.9454	1.0532
μ	-4.1596	-4.0877	-4.8311	-5.1097	-4.4691	-4.2320
ΔN	0.2865	0.3508	0.1319	-0.0532	0.5549	0.4251

efficiency on the metal surface. For an organic molecule to be considered a corrosion inhibitor, ΔN must be fewer than 3.6. If the ΔN is more than 3.6, the inhibition efficiency will drop [45]. Table 3 shows ΔN for L1 and L2 and their metal complexes are ranged of 0.0532–0.5549. The substituent groups and the chemical structure of L1 and L2 significantly impact the ΔN values. ΔN calculations indicate that the copper and nickel surfaces are considered electron-accepting molecules. While L1 and L2 are electron-donating molecules.

DFT calculations provide insights into the electronic structure of metal azo complexes, detailing the distribution of electron density, frontier molecular orbitals, and bonding interactions between the metal ion and azo ligands [42]. This information helps in understanding the stability and reactivity of the complexes. In addition, DFT calculations can predict and interpret the spectroscopic properties of metal azo complexes, including UV-vis absorption spectra and IR spectra. By simulating these spectra, DFT also can assist in assigning experimental peaks, identifying electronic transitions, and assessing the influence of different metal ions and ligand substitutions on the optical properties [43]. Moreover, DFT calculations optimize the molecular geometry of metal azo complexes, predicting bond lengths, angles, and overall molecular structure [44]. Optimized geometries provide valuable data for comparing with experimental crystallographic data and understanding the structural factors influencing properties like stability and catalytic activity. Furthermore, DFT calculations can compute thermodynamic parameters such as enthalpy, Gibbs free energy, and reaction pathways associated with the formation and decomposition of metal azo complexes [45]. This helps predict the stability of complexes under different conditions and assess their feasibility for various

applications. For example, in catalytic applications, DFT calculations elucidate reaction mechanisms involving metal azo complexes [46]. By modeling transition states and intermediate species, the DFT can identify the rate-determining steps, propose reaction pathways, and evaluate the role of the metal center and azo ligands in catalytic processes. DFT calculations also enable the rational design of new metal azo complexes with desired properties by predicting how changes in ligand structure, metal ion, or coordination environment affect their electronic, optical, and catalytic behaviors. This predictive capability accelerates the discovery and development of novel materials and catalysts [47-49].

Fig. S17-S38 present the optimized geometries, HOMO, and LUMO orbitals for studied ligands L1 (Fig. 5(a) and 5(b)) and L2, as well as their complexes. Table 3 and 4 summarize the calculated electronic properties and global reactivity parameters. Theoretical calculations showed that the $[\text{CuCl}_2\text{L}_2]$ has the lowest E_g (6.30604 eV), so it is the softest complex, and it is the best to be easily excited, while the $[\text{NiCl}_2\text{L}_1]$ has the highest E_g (7.34536 eV), so it is the hardest molecule. According to total energy calculations, the $[\text{NiCl}_2\text{L}_2]$ and $[\text{CuCl}_2\text{L}_2]$ complexes with low total energy values have better stability in comparison to $[\text{NiCl}_2\text{L}_1]$ and $[\text{CuCl}_2\text{L}_1]$ complexes. $[\text{CuCl}_2\text{L}_1]$ has the highest E_{HOMO} (−6.3165 eV), which allows them to be the best electron donor complex. On the other hand, the $[\text{CuCl}_2\text{L}_2]$ has the lowest E_{LUMO} (−2.2831 eV), which makes it the best electron acceptor complex.

The IP and EA represent the electron exchange involved in the electron-donating and accepting abilities of the complexes, respectively [36]. From Table 3, the $[\text{NiCl}_2\text{L}_2]$ complex displays the lowest ionization potential, indicating a high electron-donating ability.

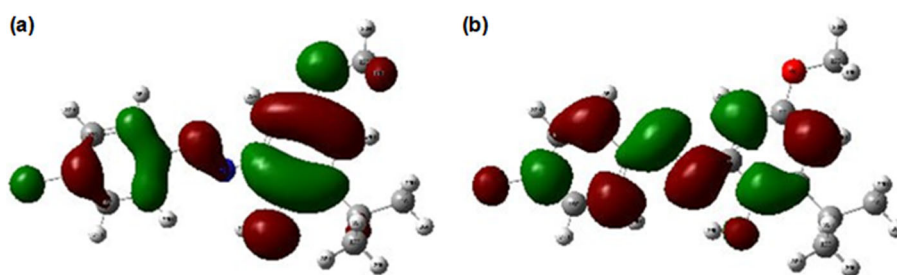


Fig 5. (a) HOMO and (b) LUMO of L1

The electron acceptor or donor properties can also be explained in terms of χ , which reflects a molecule's ability to attract electrons [44]. Results indicate the complex [CuCl₂L1] displays the highest electronegativity value and high electron acceptor complex, while the complex [CuCl₂L2] shows the lowest electronegativity value and high electron donating complex.

The complex's E_g and η follow the same trend. Complexes with low E_g and η possess low stability and more reactivity. Results indicate that the complex [NiCl₂L2] has the lowest hardness value (0.5148 eV) and is more reactive than the other complexes. The ζ and η follow a reversed trend. Hence, the complex [NiCl₂L2] has the highest value of ζ (1.9454 eV), which is expected to show less stability and the highest reactivity.

The μ value gives an idea about the charge transfer within any compound in its ground state. From the results, the complex [CuCl₂L1] has the highest μ of -5.1097 eV. Therefore, it is less stable and more reactive than the other complexes.

Corrosion Computational Studies

DFT studies have been used to compare theoretical and experimental data, such as corrosion calculations, spectroscopic measurements, and crystallographic structures, to validate theoretical predictions and refine computational models. This iterative process enhances the accuracy and reliability of both experimental and computational studies [50-51].

Quantum chemistry calculations have been used as an effective and reliable tool for studying corrosion mechanisms [44,47]. Herein, azo compounds were

studied computationally, summarized in Table 3. Table 3 display these results comparable to previous studies [35-36,44-45,47]. Quantum theoretical calculations provide essential information that cannot be collected from experimental data and highlight the experiment trend [52]. Some important structural information summarized in Table 3 include E_{HOMO} , E_{LUMO} , χ , ζ , η , ΔN , IP, dipole moment, and optimized geometries. L1 and L2, as proposed corrosion inhibitors, showed interesting electronic features such as the E_{HOMO} and E_{LUMO} values revealing the large distribution of the HOMO and LUMO orbitals on both sides of the ligands (and L2). Fig. 6(a) and 6(b) show the donor groups, such as Cl, N=N, OH, and phenyl groups. These donor groups represent adsorption centers on the surface of the compound. The general mechanism of the anticorrosion effect described in Fig. 6(a) and 6(b) occurs as adsorption on the metal surface depending on donor acceptor reactions. There are two possible adsorption interactions between the metal surface and the inhibitor that can explain anticorrosion mechanisms (Fig. 6(a) and 6(b)). The first possible interaction is chemisorption and physisorption, where the vacant d-orbital of copper (Cu) or nickel (Ni) interacts with the chlorine, oxygen (O), and nitrogen (N) atoms of the inhibitor, forming a strong bond and weak interactions. These bonds and interactions help protect the metal surface from corrosion by sharing lone-pair electrons. Secondly, a retro-donation interaction can occur between the ionized Cu and Ni atoms on the metal surface and the π -electrons of the aromatic ring in the inhibitors L1 or L2. Consequently, these interactions contribute to inhibiting

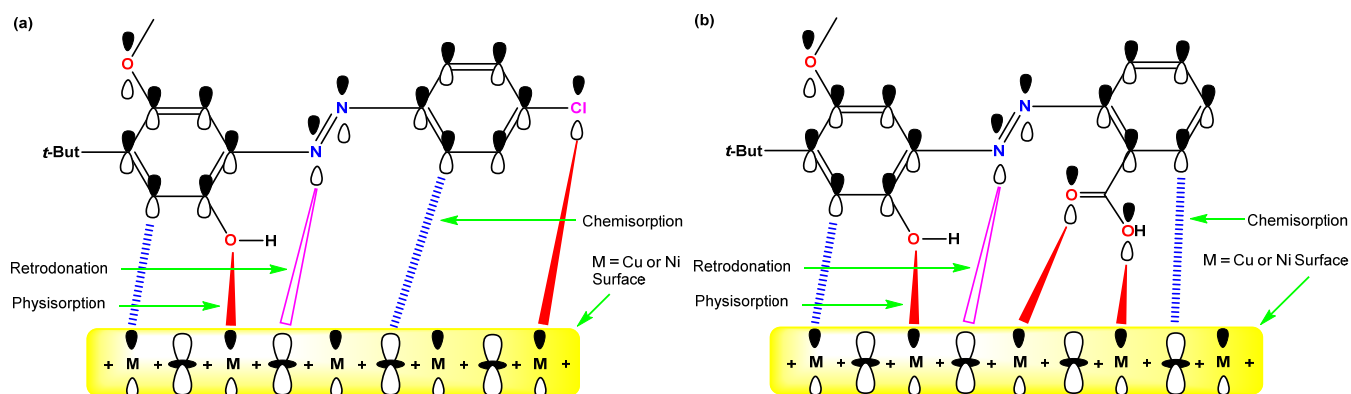


Fig 6. Proposed corrosion inhibition mechanism of inhibitor (a) L1 and (b) L2 with metal surface

the corrosion process. The adsorbed organic inhibitors (L1 or L2) also cover a large surface area, forming a protective film over the metal surface, which enhances the inhibition performance [53-55].

Computationally, anticorrosion efficiency correlated with energy gap value. According to the molecular orbitals theory, the absorption between the metal surface and the chemical compound is significantly affected by HOMO and LUMO. Decreasing the energy gap value will increase the ability to give electrons to an acceptor that has vacant orbitals and low energy, consequently increasing anticorrosion efficiency [56].

The E_g (3.0752 eV) for L1 is higher than L2 (2.7181 eV). This small difference might be because of the para-substituted (chlorine atom) as a strong electron donor group. Based on these computational results, L2 is expected to be more efficient as a corrosion inhibitor than L1. Table 3 showed an interesting increase in the energy gap for complexes 1–4 in comparison with the energy gap for L1 and L2. The coordination between metal (electron acceptor) and ligand (electron donor) will increase the energy gap. The increase in the energy gap also reflects the strong coordination between metal and ligand. Thus, complexes 1–4 are expected to be less anticorrosion efficiency than L1 and L2. Moreover, it is well known a higher dipole moment (Eq. (8)) will enhance corrosion inhibition due to the tendency of metal (Cu or Ni) as a soft acid to react with the soft base (L1 or L2), which has low hardness and high softness [57-58];

$$IE(\text{Theor}) = 123.418 - 9.334(\text{D.M}) - 0.131(\text{SE}) \quad (8)$$

where SE is the solvation energy that the Firefly Program computes, and D.M is the dipole moment.

■ CONCLUSION

The title complexes showed promising results in the theoretical and computational reactivity calculations. Highly air and thermal stable azo metal complexes [NiCl₂L1], [CuCl₂L1], [NiCl₂L2], and [CuCl₂L2] with a melting point ranging between (240–300 °C). Complexes 1–4 were synthesized in one step reaction pot by reacting L1 or L2 ligands with different metal chlorides. The compounds were chemically characterized using a set of chemical characterization techniques such as molar

electrical conductivity, FTIR, ¹H-NMR, MS spectrometry, and TGA. These analyses confirmed the purity of the prepared complexes. DFT calculations are indispensable tools for studying metal azo compounds, providing fundamental insights into their electronic structure, spectroscopic properties, stability, and reactivity. By integrating theory and computational optimization, these azo compounds for anticorrosion applications in materials science and beyond, driving innovation in diverse fields of chemistry and technology. Computational calculations showed the optimized ability of L1 and L2 as corrosion inhibitors based on determining various thermodynamic parameters and investigating the adsorption mechanism. This demonstrates that the adsorption follows the Langmuir model and is classified as chemisorption and physisorption. The anti-corrosion activity of new azo derivatives can be explored to build a comprehensive database of azo compounds as corrosion inhibitors.

■ ACKNOWLEDGMENTS

The authors gratefully acknowledge Basrah University for providing some research facilities.

■ CONFLICT OF INTEREST

The authors declare no conflict of interest.

■ AUTHOR CONTRIBUTIONS

Safaa Hussein Ali contributed to the conception and design of the study. Hanadi Mahdi Jarallah performed the experimental part and wrote the first draft. Safaa Hussein Ali performed a computational simulation and revised and edited the final draft. All authors read and approved the final version of this manuscript.

■ REFERENCES

- [1] Shimizu, T., Tanifuji, N., and Yoshikawa, H., 2022, Azo compounds as active materials of energy storage systems, *Angew. Chem. Int. Ed.*, 61 (36), e202206093.
- [2] Luo, C., Ji, X., Hou, S., Eidson, N., Fan, X., Liang, Y., Deng, T., Jiang, J., Wang, C., and Wang, C., 2018, Azo compounds derived from

- electrochemical reduction of nitro compounds for high performance Li-ion batteries, *Adv. Mater.*, 30 (23), 1706498.
- [3] Ahmad, K., Naseem, H.A., Parveen, S., Shah, H.R., Shah, S.S.A., Shaheen, S., Ashfaq, A., Jamil, J., Ahmad, M.M., and Ashfaq, M., 2019, Synthesis and spectroscopic characterization of medicinal azo derivatives and metal complexes of Indandion, *J. Mol. Struct.*, 1198, 126885.
- [4] Mezgebe, K., and Mulugeta, E., 2022, Synthesis and pharmacological activities of azo dye derivatives incorporating heterocyclic scaffolds: A review, *RSC Adv.*, 12 (40), 25932–25946.
- [5] Kamenická, B., and Kuchtová, G., 2024, Critical review on electrooxidation and chemical reduction of azo dyes: Economic approach, *Chemosphere*, 363, 142799.
- [6] Aziz, D.M., Hassan, S.A., and Aziz, S.B., 2024, Synthesis and characterization of enhanced azo-azomethine doped PANI/HCl conducting polymers for electrochemical applications, *Sci. Rep.*, 14 (1), 18122.
- [7] Selvaraj, V., Swarna Karthika, T., Mansiya, C., and Alagar, M., 2021, An over review on recently developed techniques, mechanisms and intermediate involved in the advanced azo dye degradation for industrial applications, *J. Mol. Struct.*, 1224, 129195.
- [8] Zhang, Z.Y., Dong, D., Bösking, T., Dang, T., Liu, C., Sun, W., Xie, M., Hecht, S., and Li, T., 2024, Solar azo-switches for effective E→Z photoisomerization by sunlight, *Angew. Chem. Int. Ed.*, 63 (31), e202404528.
- [9] Hadji, D., Baroudi, B., and Bensafi, T., 2024, Nonlinear optical properties of azo sulfonamide derivatives, *J. Mol. Model.*, 30 (4), 117.
- [10] Al-Hamdani, U.J., Hassan, Q.M., Mohammed, M.J., Sultan, H.A., Dhumad, A.M., Emshary, C.A., and Alharis, R.A., 2023, Synthesis and investigation of nonlinear optical properties of Azo-SR8 compound using visible laser beams, *Opt. Mater.*, 143, 114293.
- [11] Saleh, M.G.A., El-Sayed, W.A., Zayed, E.M., Shawky, M., and Mohamed, G.G., 2024, Analyzing the structure of the metal complexes of biologically active azo dye ligand, *Appl. Organomet. Chem.*, 38 (4), e7397.
- [12] Majhool, S.H., Waheeb, A.S., and Ali Awad, M., 2024, Preparation, spectral characterization, antimicrobial and cytotoxic studies of some transition metal nanocomplexes of a novel azo derivative formed from 2-amino-5-methylthiazol, *J. Nanostruct.*, 14 (2), 411–426.
- [13] Nguyen, V.A., Vu, T.N.A., Polyanskaya, N., Utenyshev, A., Shilov, G., Vasil'eva, M., Anh Tien, N., and Kovalchukova, O., 2023, Structure and properties of some S-containing azo-derivatives of 5-pyrazolone and their Cu(II), Co(II), and Ni(II) metal complexes, *Inorg. Chem. Commun.*, 158, 111648.
- [14] Khedr, A.M., Gouda, A.A., and El-Ghamry, H.A., 2022, Nano-synthesis approach, elaborated spectral, biological activity and *in silico* assessment of novel nano-metal complexes based on sulfamerazine azo dye, *J. Mol. Liq.*, 352, 118737.
- [15] Gultepe, O., and Atay, F., 2024, Investigation of structural, optical, surface, electrochemical and corrosion properties of ZnO and AZO nanorod arrays for dye absorption applications, *Opt. Mater.*, 154, 115748.
- [16] Sahar, Y.J., Mohammed, H., and Al-Abady, Z.N., 2023, Synthesis and characterization of new metal complexes containing azo-indole moiety and anti-leukemia human (HL-60) study of its palladium(II) complex, *Results Chem.*, 5, 100847.
- [17] Yang, Y., Li, Y., Lu, Y., Chen, Z., and Luo, R., 2024, A three-dimensional azo-bridged porous porphyrin framework supported silver nanoparticles as the state-of-the-art catalyst for the carboxylative cyclization of propargylic alcohols with CO₂ under ambient conditions, *ACS Catal.*, 14 (13), 10344–10354.
- [18] Ramamurthy, K., Priya, P.S., Murugan, R., and Arockiaraj, J., 2024, Hues of risk: Investigating genotoxicity and environmental impacts of azo textile dyes, *Environ. Sci. Pollut. Res.*, 31 (23), 33190–33211.

- [19] Gvoic, V., Prica, M., Turk Sekulic, M., Pap, S., Paunovic, O., Kulic Mandic, A., Becelic-Tomin, M., Vukelic, D., and Kerkez, D., 2024, Synergistic effect of Fenton oxidation and adsorption process in treatment of azo printing dye: DSD optimization and reaction mechanism interpretation, *Environ. Technol.*, 45 (9), 1781–1800.
- [20] Chauhan, K.V., Rawal, S., Patel, N.P., and Vyas, V., 2024, The impact of temperature and power variation on the optical, wettability, and anti-icing characteristics of AZO coatings, *Crystals*, 14 (4), 368.
- [21] Hamasha, M.M., Bani-Irshid, A.H., and Masadeh, A., 2024, Evaluation of thermal stresses on thin Al and AZO films deposited on polyethylene terephthalate substrates for flexible electronics applications, *Mater. Sci. Eng., B*, 299, 117056.
- [22] Bagdatli, E., and Tastemel, B., 2024, Novel azo- and bisazo-5-pyrazolone dyes and their application as a colorimetric chemosensor for naked eye recognition of Cu^{2+} , *J. Mol. Struct.*, 1314, 138765.
- [23] Ozel, K., and Yildiz, A., 2024, High-performance transparent AZO UV photodetectors, *Opt. Quantum Electron.*, 56 (7), 1258.
- [24] Bilbao Zubiri, I., and Carré, A.L., 2023, Giving a new status to a dyes collection: A contribution to the chromotope project, *Heritage*, 6 (2), 2202–2219.
- [25] Zobeidi, A., Neghmouche Nacer, S., Atia, S., Kribaa, L., Kerassa, A., Kamarchou, A., AlNoaimi, M., Ghernaout, D., Ali, M.A., Lagum, A.A., and Elboughdiri, N., 2023, Corrosion inhibition of azo compounds derived from Schiff bases on mild steel (XC70) in (HCl, 1 M DMSO) medium: An experimental and theoretical study, *ACS Omega*, 8 (24), 21571–21584.
- [26] Weng, S., Cao, Z., Song, K., Chen, W., Jiang, R., Rogachev, A.A., Yarmolenko, M.A., Zhou, J., and Zhang, H., 2024, Constructing an $\text{Al}^{3+}/\text{Zn}^{2+}$ -based solid electrolyte interphase to enable extraordinarily stable Al^{3+} -based electrochromic devices, *ACS Appl. Mater. Interfaces*, 16 (14), 18164–18172.
- [27] Yaman, M., Renklitepe, C., Kaplan, G., Sakalli, Y., Seferoğlu, N., Şahin, E., and Seferoğlu, Z., 2024, D- π -A azo dyes bearing thiazole-diphenylamine units: Synthesis, photophysical and molecular structure properties, and use for dyeing of polyester fabrics, *Dyes Pigm.*, 222, 111840.
- [28] Gupta, P.O., and Sekar, N., 2024, Photophysical properties and photostability of novel 2-amino-3-benzothiazole thiophene-based azo disperse dyes, *J. Photochem. Photobiol., A*, 457, 115924.
- [29] Brillas, E., and Oliver, R., 2024, Development of persulfate-based advanced oxidation processes to remove synthetic azo dyes from aqueous matrices, *Chemosphere*, 355, 141766.
- [30] Luo, C., Xu, G.L., Ji, X., Hou, S., Chen, L., Wang, F., Jiang, J., Chen, Z., Ren, Y., Amine, K., and Wang, C., 2018, Reversible redox chemistry of azo compounds for sodium-ion batteries, *Angew. Chem. Int. Ed.*, 57 (11), 2879–2883.
- [31] Pal, S., Guin, A.K., Chakraborty, S., and Paul, N.D., 2024, Zn(II)-stabilized azo-anion radical catalyzed sustainable C–C bond formation: Regioselective alkylation of fluorene, oxindole, and indoles, *ChemCatChem*, 16 (10), e202400026.
- [32] Mondal, B., and Mukherjee, P.S., 2018, Cage encapsulated gold nanoparticles as heterogeneous photocatalyst for facile and selective reduction of nitroarenes to azo compounds, *J. Am. Chem. Soc.*, 140 (39), 12592–12601.
- [33] Sumrit, P., Kamavichanurat, S., Joopor, W., Wattanathana, W., Nakornkhet, C., and Hormnirun, P., 2024, Aluminium complexes of phenoxy-azo ligands in the catalysis of *rac*-lactide polymerization, *Dalton Trans.*, 53 (33), 13854–13870.
- [34] Khaled, K.F., 2010, Electrochemical behavior of nickel in nitric acid and its corrosion inhibition using some thiosemicarbazone derivatives, *Electrochim. Acta*, 55 (19), 5375–5383.
- [35] Madkour, L.H., Kaya, S., and Obot, I.B., 2018, Computational, Monte Carlo simulation and experimental studies of some arylazotriazoles (AATR) and their copper complexes in corrosion inhibition process, *J. Mol. Liq.*, 260, 351–374.
- [36] Hadisaputra, S., Purwoko, A.A., Savalas, L.R.T., Prasetyo, N., Yuanita, E., and Hamdiani, S., 2020, Quantum chemical and Monte Carlo simulation

- studies on inhibition performance of caffeine and its derivatives against corrosion of copper, *Coatings*, 10 (11), 1086.
- [37] Frisch, M.J., Trucks, G.W., Schlegel, H.B., Scuseria, G.E., Robb, M.A., Cheeseman, J.R., Scalmani, G., Barone, V., Mennucci, B., Petersson, G.A., Nakatsuji, H., Caricato, M., Li, X., Hratchian, H.P., Izmaylov, A.F., Bloino, J., Zheng, G., Sonnenberg, J.L., Hada, M., Ehara, M., Toyota, K., Fukuda, R., Hasegawa, J., Ishida, M., Nakajima, T., Honda, Y., Kitao, O., Nakai, H., Vreven, T., Montgomery, J.A., Jr., Peralta, J.E., Ogliaro, F., Bearpark, M., Heyd, J.J., Brothers, E., Kudin, K.N., Staroverov, V.N., Kobayashi, R., Normand, J., Raghavachari, K., Rendell, A., Burant, J.C., Iyengar, S.S., Tomasi, J., Cossi, M., Rega, N., Millam, J.M., Klene, M., Knox, J.E., Cross, J.B., Bakken, V., Adamo, C., Jaramillo, J., Gomperts, R., Stratmann, R.E., Yazyev, O., Austin, A.J., Cammi, R., Pomelli, C., Ochterski, J.W., Martin, R.L., Morokuma, K., Zakrzewski, V.G., Voth, G.A., Salvador, P., Dannenberg, J.J., Dapprich, S., Daniels, A.D., Farkas, Ö., Foresman, J.B., Ortiz, J.V., Cioslowski, J., and Fox, D.J., 2013, *Gaussian-09 Revision D.01*, Gaussian, Inc., Wallingford, CT.
- [38] Dennington, R., Keith, T.A., and Millam, J.M., 2009, *GaussView 5.0*, Semichem Inc. Shawnee Mission, KS, US.
- [39] Hasan, N., 2024, Spectroscopy, thermal analysis, bioavailability and anticancer activity of copper(II) complex with heterocyclic azo dye ligand, *Cent. Asian J. Med. Nat. Sci.*, 5 (1), 93–105.
- [40] Abdulrazzaq, A.G., and Al-Hamdani, A.A.S., 2024, Synthesis, characterization, thermal analysis study and antioxidant activity for some metal ions Cr(III), Fe(III), Mn(II) and Pd(II) complexes with azo dye derived from p-methyl-2-hydroxybenzaldehyde, *Baghdad Sci. J.*, 21 (6), 1960.
- [41] Koopmans, T., 1934, Über die zuordnung von wellenfunktionen und eigenwerten zu den einzelnen elektronen eines atoms, *Physica*, 1 (1-6), 104–113.
- [42] Islam, N., and Chandra Ghosh, D., 2011, A new algorithm for the evaluation of the global hardness of polyatomic molecules, *Mol. Phys.*, 109 (6), 917–931.
- [43] Sharma, S.J., Khan, Z.N., Zambare, A.A., Bagal, M.S., Barshi, A.S., Rindhe, S.M., and Sekar, N., 2024, Synthesis, spectroscopic, DFT, TD-DFT, and dyeing studies of 2-amino-3-cyano thiophene-based azo dyes on wool and nylon, *Dyes Pigm.*, 228, 112209.
- [44] Hadisaputra, S., Purwoko, A.A., and Hamdiani, S., 2021, Substituents effects on the corrosion inhibition performance of pyrazolone against carbon steels: Quantum chemical and Monte Carlo simulation studies, *Int. J. Corros. Scale Inhib.*, 10 (1), 419–440.
- [45] Rodríguez, J.A., Cruz-Borbolla, J., Arizpe-Carreón, P.A., and Gutiérrez, E., 2020, Mathematical models generated for the prediction of corrosion inhibition using different theoretical chemistry simulations, *Materials*, 13 (24), 5656.
- [46] Tanaka, D., Sawai, S., Hattori, S., Nozaki, Y., Yoon, D.H., Fujita, H., Sekiguchi, T., Akitsu, T., and Shoji, S., 2020, Microdroplet synthesis of azo compounds with simple microfluidics-based pH control, *RSC Adv.*, 10 (64), 38900–38905.
- [47] Oukhrib, R., Abdellaoui, Y., Berisha, A., Abou Oualid, H., Halili, J., Jusufi, K., Ait El Had, M., Bourzi, H., El Issami, S., Asmary, F.A., Parmar, V.S., and Len, C., 2021, DFT, Monte Carlo and molecular dynamics simulations for the prediction of corrosion inhibition efficiency of novel pyrazolynucleosides on Cu(111) surface in acidic media, *Sci. Rep.*, 11 (1), 3771.
- [48] Dembitsky, V.M., Glorizova, T.A., and Poroikov, V.V., 2017, Pharmacological and predicted activities of natural azo compounds, *Nat. Prod. Bioprospect.*, 7, 151–169.
- [49] Velasco, M.I., Kinen, C.O., Hoyos de Rossi, R., and Rossi, L.I., 2011, A green alternative to synthesize azo compounds, *Dyes Pigm.*, 90 (3), 259–264.
- [50] Tassaoui, K., Damej, M., Molhi, A., Berisha, A., Errili, M., Ksama, S., Mehmeti, V., El Hajjaji, S., and Benmessaoud, M., 2022, Contribution to the corrosion inhibition of Cu-30Ni copper-nickel alloy by 3-amino-1,2,4-triazole-5-thiol (ATT) in 3% NaCl solution. Experimental and theoretical study

- (DFT, MC and MD), *Int. J. Corros. Scale Inhib.*, 11 (1), 221–244.
- [51] Ali, S.H., Mohammed, S.S., Obaid, H.T., and Gamagedara, S., 2024, Syntheses, characterisation, thermal analysis and theoretical studies of some imino ethanone metal complexes, *Baghdad Sci. J.*, 21 (12), 3661–3672.
- [52] Obaid, H.T., Mutar, M.M., and Ali, S.H., 2025, Sulfasalazine as a corrosion inhibitor on carbon steel metal surfaces in acidic media using the hydrogen evolution method: Experimental and theoretical studies, *Indones. J. Chem.*, 25 (1), 90–99.
- [53] Khudhair, Z.T., and Shihab, M.S., 2022, Study of some azo derivatives as corrosion inhibitors for mild steel in 1 M H₂SO₄, *Surf. Eng. Appl. Electrochem.*, 58 (6), 708–719.
- [54] Dhaef, H.K., Al-Asadi, R.H., Shenta, A.A., and Mohammed, M.K., 2021, Novel bis maleimide derivatives containing azo group: Synthesis, corrosion inhibition, and theoretical study, *Indones. J. Chem.*, 21 (5), 1212–1220.
- [55] Albo Hay Allah, M.A., Balakit, A.A., Salman, H.I., Abdulridha, A.A., and Sert, Y., 2023, New heterocyclic compound as carbon steel corrosion inhibitor in 1 M H₂SO₄, high efficiency at low concentration: Experimental and theoretical studies, *J. Adhes. Sci. Technol.*, 37 (3), 525–547.
- [56] Murmu, M., Murmu, N.C., Ghosh, M., and Banerjee, P., 2022, Density functional theory, Monte Carlo simulation and non-covalent interaction study for exploring the adsorption and corrosion inhibiting property of double azomethine functionalised organic molecules, *J. Adhes. Sci. Technol.*, 36 (23-24), 2732–2760.
- [57] Abdou, M.M., Younis, O., and El-Katori, E.E., 2022, Synthesis, experimental and theoretical studies of two aryl-azo derivatives clubbed with 2-acetylphenol and their application as novel luminescent coatings with high anticorrosion efficiency, *J. Mol. Liq.*, 360, 119506.
- [58] Mustafa Mamad, D., Hussein Azeez, Y., Khalid Kaka, A., Mahmood Ahmed, K., Anwar Omer, R., and Omer Ahmed, L., 2024, The inhibitor activity of some azo compound derivatives using density functional theory and molecular dynamics simulations, *Comput. Theor. Chem.*, 1237, 114645.